The cage elasticity and under-field structure of concentrated magnetic colloids probed by small angle X-ray scattering

Elie Wandersman, Andrejs Cēbers, Emmanuelle Dubois, Guillaume Mériguet, Aymeric Robert, Régine Perzynski

Soft Matter

RSC Publishing

PAPER

View Article Online
View Journal | View Issue

The cage elasticity and under-field structure of concentrated magnetic colloids probed by small angle X-ray scattering

Cite this: *Soft Matter*, 2013, **9**, 11480

E. Wandersman,[ab] A. Cēbers,[c] E. Dubois,[a] G. Mériguet,[a] A. Robert[de] and R. Perzynski*[a]

In the present study we probe the bulk modulus and the structure of concentrated magnetic fluids by small angle X-ray scattering. The electrostatically stabilized nanoparticles experience a repulsive interparticle potential modulated by dipolar magnetic interactions. On the interparticle distance length scale, we show that nanoparticles are trapped under-field in oblate cages formed by their first neighbours. We propose a theoretical model of magnetostriction for the field-induced deformation of the cage. This model captures the anisotropic features of the experimentally observed scattering pattern on the local scale in these strongly interacting colloidal dispersions.

Received 18th July 2013
Accepted 16th October 2013

DOI: 10.1039/c3sm51961a

www.rsc.org/softmatter

1. Introduction

Numerous applications of magnetic fluids, such as seals or field-assisted dampers,[1–4] require concentrated products. Such concentrated magnetic colloids are also model systems, as the magnetic field is a powerful and tunable external parameter, controlling for example the geometric conformations of magnetic foams.[5,6] The knowledge of the under-field structure of these magnetic colloids is mandatory. They are dipolar fluids based on monodomain magnetic nanoparticles (NPs) dispersed in a liquid carrier with stabilization against aggregation performed either with a steric coating or with an electrostatic double layer (in polar carriers).[3,4] When the dipolar interaction is dominant, the nanoparticles self-assemble under the field into anisotropic structures,[7] driven by the formation of dipolar chains with NPs on contact and attracted together to produce column formation (like in non-Brownian electrorheologic fluids[8]). In contrast when the interparticle repulsion is dominating as in the present work, the dipolar interaction (which can be tuned by applying a magnetic field through the progressive alignment of the NP permanent magnetic moment) only modulates the liquid-like structural organization of the magnetic fluid.[9,10] Concentrated magnetic fluids then present an under-field structure with anisotropic features of the structure factor $S(\vec{q})$,[9,11–13] both on macroscopic scales (at low scattering vectors $\vec{q}$) and on the local scale close to $S(\vec{q})$ maxima at $\vec{q}^{\max}$. The low q anisotropy of $S(\vec{q})$ is well explained. It has been extensively described with a mean field model[11,14,15] and with a mean spherical model.[16] We focus here on the anisotropy of $S(\vec{q})$ around its maximum and first of all, on the anisotropy of $q^{\max}$ itself. This corresponds to the length scale of the cages made by the first neighbours, which entrap the NPs. Numerical simulations of dipolar soft sphere fluids[17] predict in that case an anisotropic local organization of the NPs more structured along the field than perpendicularly to the field, forming column-like structures inside the liquid carrier. Previous experimental studies[9,11,12] performed by Small Angle Neutron Scattering (SANS) have evidenced an opposite behavior with a structure more marked in the direction perpendicular to the field. However these SANS experiments were not able to evidence any anisotropy of the mean interparticle position (anisotropy of $q^{\max}$). Thanks to the much better spatial resolution of Small Angle X-ray Scattering (SAXS), the measurements presented here show a clear anisotropy of $q^{\max}$. We present here a simple model based on the field-induced magnetostriction of the NP cages at constant volume. It allows reproduction of the anisotropy of $q^{\max}$ and $S(q^{\max})$, experimentally measured by SAXS.

After giving the details of our experiment in Section 2, we present in Section 3 the zero field experimental results concerning NP cages and the bulk modulus B_0 of the magnetic fluids in zero field, together with the NP mean quadratic displacement in their cage. The field-induced results are then presented in Section 4 before describing our theoretical model in Section 5. It is then compared with respect to the experimental results in Section 6. Its limitations are then discussed in Section 7.

[a]*UPMC – Lab. PECSA – UMR 7195 CNRS-UPMC-ESPCI, case 51, 4 place Jussieu, F-75005 Paris, France. E-mail: regine.perzynski@upmc.fr*

[b]*UPMC – Lab. Jean Perrin – FRE 3231 CNRS-UPMC, case 114, 4 place Jussieu, F-75005 Paris, France*

[c]*University of Latvia, Zellu-8, Riga, LV-1002, Latvia*

[d]*European Synchrotron Radiation Facility, 6 rue Jules Horowitz BP 220, F-38043 Grenoble Cedex 9, France*

[e]*SLAC National Accelerator Laboratory, Linac Coherent Light Source, 2575 Sand Hill Rd, Menlo Park, CA 94025, USA*

2. Materials and methods

2.1. Samples

The magnetic fluids studied here are prepared as described in ref. 9 and 18. They consist of aqueous dispersions of maghemite (γ-Fe_2O_3) nanoparticles (typically 10 nm in diameter) coated with citrate molecules to ensure a negative surface charge at pH = 7 ($\sim 2e^-$ per nm^2).[19] The interaction between NPs is composed of (i) van der Waals attraction, (ii) electrostatic repulsion that can be screened by the presence of free ions in the solution, and (iii) anisotropic dipolar interaction between the magnetic moments $\vec{\mu}$ of the NPs which are magnetic monodomains. A chemical control of the dispersions allows an increase of the strength of electrostatic repulsion leading to the colloidal stability of the magnetic fluid.[13,20]

The NP size polydispersity at the end of the chemical synthesis is reduced thanks to a size-sorting process.[21,22] We retain the largest nanoparticles among the synthesis batch in order to obtain a rather large magnetic dipolar interaction. High NP concentrations at fixed ionic strength are obtained thanks to the osmotic stress.[9,18] The citrate species adsorbed on the NPs are in equilibrium with free citrate species. The concentration of these free species $[cit]_{free}$ is fixed in the dialysis bath in order to create a strong enough electrostatic repulsion to maintain the colloidal stability of the magnetic fluid under an external magnetic field. We therefore do not observe any demixing in two phases here[20,23,24] but we can observe an anisotropy of interaction in the small angle scattering spectra.[9] Most of the samples probed here are fluid samples, however one (sample B, see Table 1) is close to the colloidal glass transition.[18,25,26] The NP volume fraction Φ in each sample is given in Table 1 – together with $[cit]_{free}$ and the NP magnetic characteristics obtained by magnetization measurements at room temperature. d^0_{NP} is the median NP diameter and s is the polydispersity index of the log-normal distribution of d_{NP}, diameters of magnetic NPs (for small s, the standard deviation of d_{NP} distribution is close to sd^0_{NP}). d^0_{NP} and s are experimentally determined from the adjustment of MF magnetization at low volume fractions by a Langevin function weighted by the log-normal distribution of diameters,[1] with a NP saturation magnetization $m_s = 3 \times 10^5$ A m^{-1}. $M^{sat}_{MF} = m_s\Phi$ is the saturation magnetization of the different MF samples at the volume fraction Φ. The dipolar interaction parameter Ψ_{dd} (characteristic of the NPs and defined as $\Psi_{dd} = \gamma/\Phi = \frac{\mu_0}{k_B T} {m_s}^2 \frac{\pi}{6} {d_{NP}}^3$ – see Appendix I) is experimentally determined in low fields by the measurement of the initial magnetic susceptibility at low volume fractions.[9,11–13,15] Note that, comparing sample A and sample E in Table 1, a small difference in s with the same d^0_{NP} value induces a large difference in Ψ_{dd} and thus in physical properties of the sample.

Table 1 Chemical and magnetic characteristics of the samples (see the text). They are in the fluid phase except sample B which is a freshly prepared glass forming sample (see ref. 18)

Samples	$[cit]_{free}$ (M)	d^0_{NP} (nm)	s	Ψ_{dd}	Φ	M^{sat}_{MF} (kA m^{-1})
A – fluid	0.03	9.5	0.35	56	17.5%	53
B – glassy	0.03	9.5	0.35	56	30%	90
C – fluid	0.03	9.8	0.25	34	12.5%	38
D – fluid	0.01	8.5	0.35	44	16%	48
E – fluid	0.01	9.5	0.4	80	13%	39

2.2. Experimental details

SAXS experiments are realized at the ID02 beamline at the European Synchrotron Radiation Facility (Grenoble – France) using 12 keV X-rays and two sample-to-detector distances. It gives access to scattering vectors in the range 5×10^{-3} Å$^{-1} \leq q \leq 2 \times 10^{-1}$ Å^{-1} with an accuracy $\delta q = \pm 5 \times 10^{-5}$ Å^{-1}. The intensity is detected on a FReLON CCD. The samples are prepared in 1 mm diameter quartz-capillaries. A uniform magnetic field H, normal to the X-ray beam in the horizontal scattering plane, can be applied with an intensity ranging from 0 to 800 kA m^{-1}. The spectra are analyzed as in ref. 9 leading in zero field to the structure factor $S_0(q, \Phi)$ from a radial analysis of the isotropically scattered intensity. It presents a maximum at intermediate q marking the most probable interparticle distance in the isotropic dispersion. Under-field the scattering pattern is anisotropic. The intensity is thus analyzed over angular sectors of 20° width both along the field leading to $S_{||}(q, \Phi, H)$ or perpendicular to the field leading to $S_{\perp}(q, \Phi, H)$ (see ref. 9). This is illustrated in Fig. 1 which presents the SAXS

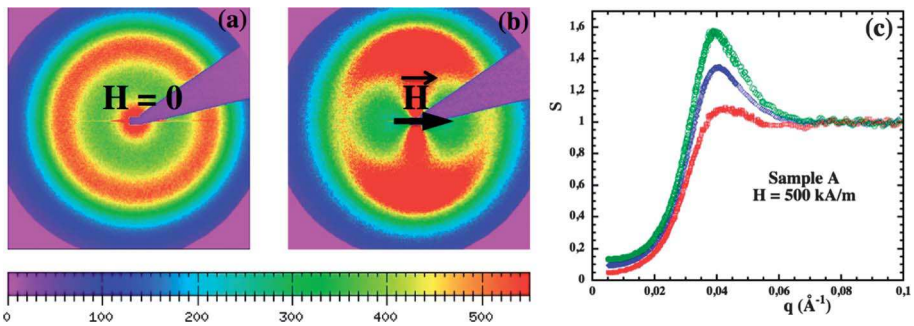

Fig. 1 SAXS patterns of sample A with $\Phi = 17.5\%$ in zero field (a) and under a magnetic field ((b) at $H = 500$ kA m^{-1}). Their associated structure factors are presented in (c); the middle curve $S_0(q)$ from (a); field induced structure factors are deduced from the analysis of (b) pattern over ±10° sectors respectively centered along the axis $\vec{q} \parallel \vec{H}$ ($S_{||}(q)$ – lower curve) and the axis $\vec{q} \perp \vec{H}$ ($S_{\perp}(q)$ – upper curve).

patterns of sample A (see Table 1) in zero field and under a field of 500 kA m^{-1}, together with the associated structure factors. Under the field, the structure factors $S_{||}(q)$ and $S_{\perp}(q)$ are deduced from the analysis of the pattern over sectors respectively centered along the axis $\vec{q} \parallel \vec{H}$ and the axis $\vec{q} \perp \vec{H}$. In both directions the liquid-like structure factor presents a maximum respectively located at $q_{\parallel}^{max}$ and $q_{\perp}^{max}$.

In the following Section, we first compare the experimental results in zero field with SANS data[9,27–29] obtained under similar conditions either on PAXY at reactor Orphée – LLB – Saclay – France or on D22 at ILL – Grenoble – France.

3. Experimental results in zero field

We first focus on the zero-field elastic properties of the magnetic fluid obtained at low q's and on the structure factor shape determined over the whole q-range.

3.1. Bulk modulus in zero field

Magnetic fluids are compressible colloidal dispersions of magnetic NPs and the bulk modulus B_0 of the NP's system can be determined experimentally by SAXS and SANS. It is related to the measured isothermal compressibility $\chi_{T,0}$ of the magnetic fluid in zero field[9,11] through

$$\chi_{T,0} = S_0(q=0) = \frac{1}{{d_0}^3}\frac{k_B T}{B_0} \quad (1)$$

where d_0 is the mean interparticle distance. When the system is in the strongly repulsive regime, then q_0^{max} scales as $\Phi^{1/3}$ and $d_0 = 2\pi/q_0^{max}$.

Introducing the mean quadratic displacement σ_0 of the nanoparticles, we obtain

$${\sigma_0}^2 = \frac{k_B T}{d_0 B_0}. \quad (2)$$

with

$$\chi_{T,0} = \left(\frac{\sigma_0}{d_0}\right)^2. \quad (3)$$

Fig. 2 shows the experimental measurements of q_0^{max} and $\chi_{T,0}$ for the samples A, B and C of Table 1 and compares them with previously published SANS results[9,27–29] with the same NP's and $[cit]_{free}$. Fig. 2a shows that the NP's system is indeed strongly repulsive here as q_0^{max} scales as $\Phi^{1/3}$. Note in Fig. 2b that $\chi_{T,0}$ can be described up to $\Phi \sim 20\%$ by the Carnahan–Starling formalism developed in Appendix II while replacing Φ with an effective volume fraction Φ_{eff} taking in account the screening length of the electrostatically charged NP's. Above Φ of the order of 12%, $\chi_{T,0}$ becomes smaller than 0.1 and thus the NPs dispersion is only weakly compressible in zero field.

Fig. 3 presents the Φ-dependence of d_0, σ_0 and B_0 deduced from Fig. 2 using eqn (1)–(3). While both d_0 and σ_0 progressively decrease with Φ, B_0 increases by two orders of magnitude over the whole range of volume fractions Φ. Let us note in Fig. 3a that if at low Φ the interparticle distance d_0 and the mean quadratic displacement σ_0 of NPs are of the same order, it is no more the case at large Φ's. When the system is becoming glassy (here for $\Phi \gtrsim 30\%$ (ref. 9 and 18)) we observe that $\sigma_0/d_0 \lesssim 0.2$ but also that B_0 does not present any strong discontinuity. It smoothly becomes of the order of 10^5 Pa, which is also the order of magnitude of the osmotic pressure of the NP's system.

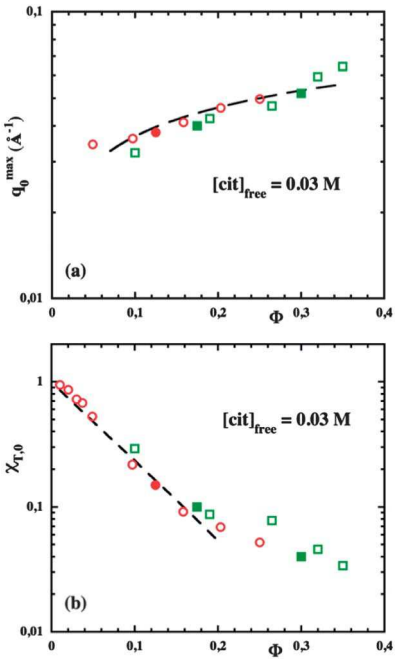

Fig. 2 Φ-dependence of q_0^{max} (a) and $\chi_{T,0}$ (b) as deduced either from SANS (open symbols) or SAXS measurements (full symbols) for the series of samples from ref. 9 and 27–29, which are based on the same magnetic NPs and prepared at the same $[cit]_{free}$ as samples A, B and C of Table 1; squares correspond to the same NPs as samples A and B; discs correspond to the same NPs as sample C. Dashed line of (a): adjustment of $q_0^{max}(\Phi)$ with $q_0^{max} = 0.1(\Phi/2)^{1/3}$ corresponding to $d_0 = 2\pi/q_0^{max}$ and $\Phi = \pi {d_{NP}}^3/6{d_0}^3$ with $d_{NP} = 9.8$ nm; dashed line of (b): adjustment of $\chi_{T,0}(\Phi)$ with the Carnahan–Starling formalism of Appendix II.

The values of d_0, σ_0 and B_0 resulting from the analysis of the SAXS spectra of samples in Table 1 are summarized in Table 2. Samples with similar volume fractions (A and D on the one hand and C and E on the other hand – see Table 1) present close B_0 values, independently from $[cit]_{free}$. The B_0 value of the glass-forming sample B can be compared with that obtained for glass-forming systems based on different microscopic objects. Indeed we can rewrite eqn (1) as $\chi_{T,0} = \frac{1}{(d_{NP}^0)^3}\frac{\Phi k_B T}{B_0}$. At equivalent $\frac{1}{\Phi}\frac{\chi_{T,0}}{k_B T}$, B_0 should scale as the inverse of the volume of the dispersed objects. The value $B_0 = 6.2 \times 10^4$ Pa found here scales well with the elastic modulus of the suspension of micron sized silica particles close to the glass transition at 0.1 Pa given in ref. 30 since the ratio of the characteristic sizes for these two systems is approximately equal to 100.

3.2. Paracrystal structure in zero field

Another way to determine the NP's mean quadratic displacement and the bulk elastic modulus is to adjust the zero-field structure factor $S_0(q)$ of the dispersions by the following

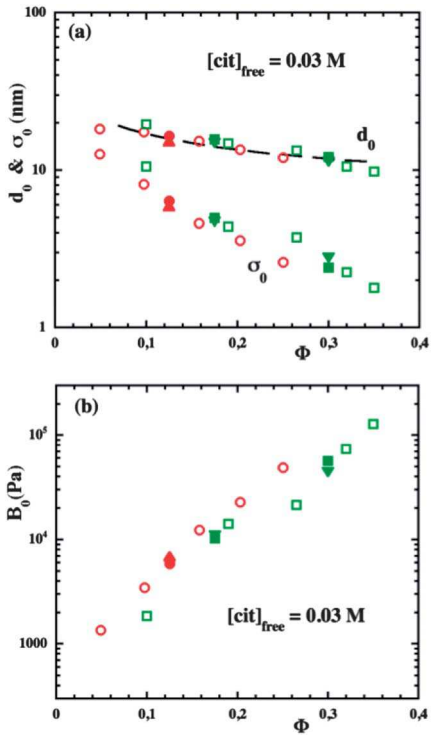

Fig. 3 Φ-dependence of d_0, σ_0 (a) and B_0 (b) deduced from the data of Fig. 2 – the same symbols as in Fig. 2; $\bar{d}$, $\bar{\sigma}_0$ (a) and $\bar{B}_0$ (b) deduced from the analysis of SAXS profiles $S(q)$ by eqn (4) for samples A, B (full downward triangles) and C (full upward triangle). Dashed line in (a) corresponds to $d_0(\text{nm}) = 9.8(\pi/6\Phi)^{1/3}$ (the same adjustment as in (b)).

expression standardly used for colloidal dispersions of (monodisperse) nanoparticles:[31]

$$S(q) = \frac{\sinh(\bar{\sigma}_0^2 q^2/2)}{\cosh(\bar{\sigma}_0^2 q^2/2) - \cos(q\bar{d})} \quad (4)$$

where $\bar{d}$ is a parameter, which equals $d_0 = 2\pi/q_0^{\max}$ only if $\bar{\sigma}_0/\bar{d} \ll 1$. We call $\bar{\sigma}_0$ and $\bar{B}_0$ the NP's mean quadratic displacement and the bulk elastic modulus determined by this method. Eqn (4) has been used for example for describing the structure of latex solutions[31] or the fluctuations of multivalent ions adsorbed on a linear polyelectrolyte chain.[32,33] With eqn (4) the compressibility expresses as $S(q=0) = (\bar{\sigma}_0/\bar{d})^2$.

In the present case, the condition $\bar{\sigma}_0/\bar{d} \ll 1$ is not always fulfilled and $\bar{d}$ has to be fitted. Therefore $S(q)$ is rewritten as a function of the two parameters $\bar{\sigma}_0/\bar{d}$ and $q\bar{d}$ which are both adjusted, $\bar{\sigma}_0/\bar{d}$ controlling the shape of $S(q)$ and $q\bar{d}$ controlling the position of the $S(q)$ maximum. The values of $\bar{\sigma}_0$ and $\bar{B}_0$ obtained with such fits are summarized in Table 2 and plotted in Fig. 3. They are rather close to the values previously obtained from $\chi_{T,0}$ and $q_0^{\max}$. Fig. 4 shows the quality of the adjustment of $S_0(q)$ with eqn (4) for samples A and C.

Despite the fact that eqn (4) does not take into account the polydispersity of the NPs, we can show a very good self-consistency between the measurements of various parameters for the system in zero field from either the $S(q)$ profile adjustment or from the compressibility determination at low q's. Indeed this model is essentially a "first neighbor" model which is weakly sensitive to polydispersity. Besides, the polydispersity which does not appear here explicitly, is hidden in the same way for both kinds of measurements through the adjustments to $q_0^{\max}$ and $S(q=0)$.

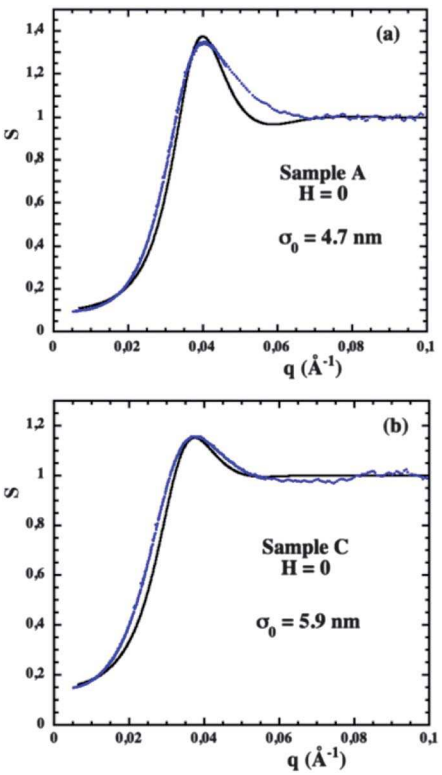

Fig. 4 Zero-field $S(q)$ profiles of sample A (a) and sample C (b) adjusted with eqn (4) (solid line) with respectively $(\bar{\sigma}_0/d_0)^2 = 0.09$ and 0.125.

Table 2 Characteristics of the samples deduced from SAXS measurements; d_0 is the mean interparticle distance in zero field and $\chi_{T,0}$ is the experimental isothermal compressibility; σ_0 and B_0 are experimentally deduced from d_0 and $\chi_{T,0}$ using eqn (1)–(3); $\bar{d}$, $\bar{\sigma}_0$ and $\bar{B}_0$ are deduced from the adjustment of $S(q)$ with eqn (4); The under-field interparticle distances $\tilde{d}_{\parallel} = d_{\parallel}(H_{\max})$ and $\tilde{d}_{\perp} = d_{\perp}(H_{\max})$ are deduced from $q_{\max}$ values at the maximum field; K_H^{el} is deduced from the under-field model in Section 5 (eqn (20), Fig. 6) and the magnetic characteristics in Table 1

Sample	d_0 (nm)	$\chi_{T,0}$	σ_0 (nm)	B_0 (Pa)	$\bar{d}$ (nm)	$\bar{\sigma}_0$ (nm)	$\bar{B}_0$ (Pa)	$\tilde{d}_{\parallel}$ (nm)	$\tilde{d}_{\perp}$ (nm)	K_H^{el} (Pa)
A	15.7	0.1	5.0	1.0×10^4	14.9	4.7	1.1×10^4	14.8	16.2	2.6×10^4
B	11.7	0.04	2.3	6.2×10^4	11.3	2.8	4.4×10^4	11.1	12	9.4×10^4
C	16.7	0.15	6.5	5.7×10^3	15.2	5.9	6.9×10^3	16.2	17	2.7×10^4
D	17.6	0.06	4.3	1.2×10^4	17	4.8	1.0×10^4	16.1	18.3	1.7×10^4
E	22.2	0.05	5.0	7.3×10^3	21.4	6.0	5.0×10^3	20.9	22.8	1.4×10^4

4. Under-field results

The scattering profiles present a strong anisotropy when an external magnetic field is applied (*cf.* Fig. 1). We focus here on the analysis of the structure factor in the directions parallel and perpendicular to the field.

First of all we find that experimentally $q_{\parallel}^{\max}(H)$ is always larger than $q_{\perp}^{\max}(H)$, meaning that the interparticle distance $d_{\parallel} = 2\pi/q_{\parallel}^{\max}$ is always smaller than $d_{\perp} = 2\pi/q_{\perp}^{\max}$. If the cage formed by the first neighbours around a given nanoparticle is approximated by an ellipsoid, this means that the zero-field spherical cage always deforms under-field as an oblate ellipsoid. Moreover at the first order, the deformation of this cage occurs at a constant volume. Indeed experimentally the ratio $d_{\parallel}(H)\,{d_{\perp}}^2(H)/{d_0}^3$ is found to be equal to 1 ± 0.02 for every applied field and whatever the sample.

Fig. 5 shows for sample A the field dependence of $q_{\parallel}^{\max}$ and $q_{\perp}^{\max}$ and that of $S_{\parallel}^{\max}$ and $S_{\perp}^{\max}$. Their under-field anisotropy goes in opposite ways and saturates in high fields. The values of $\tilde{d}_{\parallel} = d_{\parallel}(H_{\max}) = 2\pi/q_{\parallel}^{\max}(H_{\max})$ and $\tilde{d}_{\perp} = d_{\perp}(H_{\max}) = 2\pi/q_{\perp}^{\max}(H_{\max})$ are reported in Table 2.

5. Theoretical model

In these dispersions, each NP bears a permanent magnetic dipole $\vec{\mu}$. If the dispersion is dilute, the magnetization M_{MF} can be described by a Langevin formalism and results from the progressive reduction of the orientational fluctuations of the magnetic dipole $\vec{\mu}$ around the direction of the applied field $\vec{H}$. In a concentrated dispersion, these dipoles interact together through the magnetic dipolar interaction. Between two parallel dipoles $\vec{\mu}$ at distance d from each other, this dipolar interaction is anisotropic and manifests itself as attractive along the direction of the magnetic dipoles and repulsive in the perpendicular direction. It can be written at the first order as:

$$u_{\mathrm{dd}}^{\parallel} = -\frac{\mu_0\mu^2}{2\pi d^3} \quad \text{and} \quad u_{\mathrm{dd}}^{\perp} = \frac{\mu_0\mu^2}{4\pi d^3} \tag{5}$$

The model of Appendix I (from ref. 11 and 15) describes the H-dependence of M_{MF} in concentrated magnetic fluids. Under an applied field, the dipolar interaction induces a uniaxial stress between NP's, leading to a magnetostriction at constant volume, without compression. Macroscopically the magnetostrictive contribution to the energy density of the magnetic colloid may be obtained considering the total field acting on the dipoles, as in the mean field model of ref. 14. This latter model describes well the effect of the dipolar interaction on the thermodynamic properties of the magnetic colloids that are measured in the limit of $q \to 0$.[9,11,15] On a more local scale, each NP in a concentrated magnetic fluid can be seen as entrapped in a cage constituted by its first neighbouring NPs. Because of the field-induced magnetostriction, the cage around a magnetic NP, while keeping a constant volume, becomes anisotropic with a dimension $d_{||}$ smaller than $d_{\perp}$. Considering the experimental observations described in Section 4, we approximate the cage by an oblate ellipsoid of eccentricity e and constant volume $V_{\mathrm{cage}} = \frac{\pi}{6} d_{\parallel} {d_{\perp}}^2 \simeq \frac{\pi}{6} {d_0}^2$, with its symmetry axis along its magnetization $\vec{M}_{\mathrm{cage}}$. Inside the ellipsoidal cage, $\vec{M}_{\mathrm{cage}}$ is assumed to be homogeneous and each cage is associated with a magnetic moment $\vec{m}$, mean projection along $\vec{H}$ of the fluctuating moment $\vec{\mu}$ in the cage. $\vec{m}$ is field dependent with $m(H) = M_{\mathrm{MF}}(H) d_{\parallel} {d_{\perp}}^2 = M_{\mathrm{cage}}(H) V_{\mathrm{cage}}$. The energy per particle associated with the demagnetizing field is then:

$$E = -\frac{\mu_0}{2} N(e) {M_{\mathrm{cage}}}^2 V_{\mathrm{cage}} \tag{6}$$

where μ_0 is the vacuum permeability and $N(e)$ is the demagnetizing factor of the ellipsoidal cage. At small deformations (the z axis is along the direction of the magnetization; x and y axes are perpendicular to it), the eccentricity of the oblate ellipsoid is:

$$e^2 = (u_{x,x} + u_{y,y}) - 2u_{z,z} \tag{7}$$

where $\vec{u} = (u_x, u_y, u_z)$ is the displacement vector with respect to $H = 0$ position, the second subscript of $u_{i,i}$ denoting the partial derivative with respect to the corresponding variable of u_i. Accounting for the expression of the demagnetizing factor of an ellipsoid of small eccentricity:

$$N(e) = \frac{1}{3}\left(1 + \frac{2}{5} e^2\right), \tag{8}$$

and neglecting the constant term, we obtain the magnetostriction energy:

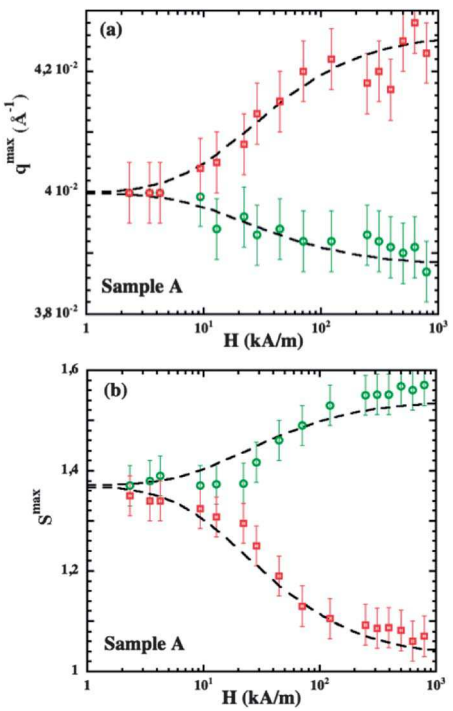

Fig. 5 Field dependence of $q_{\parallel}^{\max}$ and $q_{\perp}^{\max}$ (a) and of $S_{\parallel}^{\max}$ and $S_{\perp}^{\max}$ (b) for (fluid) sample A (the same sample as in Fig. 1 – see characteristics in Table 1). Symbols: squares in the direction parallel to the applied field and circles in the perpendicular direction. The dashed lines (see Section 6) correspond to best adjustments of the data to eqn (20) and (22) using for M_{MF} the effective mean field model of Appendix I with $d_{\mathrm{NP}} = 11.5$ nm. It leads to $K_H^{\mathrm{el}} = 2.6 \times 10^4$ Pa.

$$E_{\mathrm{m}} = \frac{4\mu_0}{5\pi} {M_{\mathrm{MF}}}^2 {d_0}^3 \left(u_{z,z} - \frac{1}{2}\left(u_{x,x} + u_{y,y}\right)\right). \quad (9)$$

In the absence of overall under-field compression ($\Delta V_{\mathrm{cage}}/V_{\mathrm{cage}} = 0$ and thus $\Sigma_i u_{i,i} = 0$ whatever H) $u_{z,z} = -(u_{x,x} + u_{y,y})$, eqn (9) has thus a form equivalent to that of the magnetostriction energy considered in ref. 34 in the case of the ferromagnetics. For the present uniaxial deformation along the z axis let us note $u_{z,z} = (z_{j+1} - z_j - d_0)/d_0$, with z_j being the average position of the j^{th} particle along the z axis. We obtain for the energy per particle

$$E_{\mathrm{m}} = \frac{6\mu_0}{5\pi} {M_{\mathrm{MF}}}^2 {d_0}^2 \left(z_{j+1} - z_j - d_0\right). \quad (10)$$

Eqn (10) is close to the energy $U_{\mathrm{dd}}^{\parallel}$ of two parallel dipoles with the radius vector along their magnetic moment $\vec{m}$:

$$U_{\mathrm{dd}}^{\parallel} = -\frac{\mu_0 m^2(H)}{2\pi\left(z_{j+1} - z_j\right)^3} \simeq -\frac{\mu_0 m^2}{2\pi {d_0}^3} + \frac{3\mu_0 m^2}{2\pi {d_0}^4}\left(z_{j+1} - z_j - d_0\right) \quad (11)$$

Here the magnetic moment $\vec{m}$ being field-dependent with $m(H) = {d_0}^3 M_{\mathrm{MF}}(H)$, we see that the magnetostrictive part of eqn (11), except for a coefficient of 0.8, coincides with the general eqn (10). Further on we use the estimate given by eqn (11).

In concentrated fluid samples the under-field interaction at the mean distance d between the colloidal particles is related to the elastic deformation of their surroundings. Denoting the mean quadratic displacement of the particles around their mean position under-field by ${\sigma_H}^2$ and assuming that it does not depend on the field value nor on its direction, we have for the global energy of a sequence of N particles along the field direction:

$$\frac{E_H}{k_{\mathrm{B}}T} = \sum_{j=0}^{N-1}\left(\frac{1}{2{\sigma_H}^2}\left(z_{j+1} - z_j - d_0\right)^2 + \frac{3\mu_0 m^2(H)}{2\pi k_{\mathrm{B}} T {d_0}^4}\left(z_{j+1} - z_j - d_0\right)\right). \quad (12)$$

Providing that $3\mu_0 m^2(H){\sigma_H}^2 \ll 4\pi k_{\mathrm{B}} T {d_0}^5$, the effective energy of the particle interaction in the sequence of N particles can be rewritten in these terms:

$$\frac{E_H}{k_{\mathrm{B}}T} = \frac{1}{2{\sigma_H}^2}\sum_{j=0}^{N-1}\left(z_{j+1} - z_j - d_{\parallel}\right)^2 + \mathrm{const} \quad (13)$$

with

$$d_{\parallel} = d_0\left(1 - \frac{3\mu_0 m^2(H){\sigma_H}^2}{2\pi k_{\mathrm{B}} T {d_0}^5}\right) \quad (14)$$

giving the renormalization of the mean distance between the particles due to the magnetostriction. Eqn (13) leads to the under-field elastic energy per unit volume

$$e_{\mathrm{elas},H} = \frac{1}{2}\frac{k_{\mathrm{B}}T}{{\sigma_H}^2 d_0} {u_{z,z}}^2 \quad (15)$$

and gives, in a way similar to eqn (2), the following estimate for the under-field elastic modulus K_H^{el}:

$$K_H^{\mathrm{el}} = \frac{k_{\mathrm{B}}T}{{\sigma_H}^2 d_0}. \quad (16)$$

K_H^{el} is analogous to a Young's modulus in this anisotropic elastic medium. It is different from the compression modulus B_0 measured at $H = 0$. We thus obtain:

$$\frac{d_{\parallel}}{d_0} = 1 - \frac{3\mu_0 {M_{\mathrm{MF}}}^2}{2\pi K_H^{\mathrm{el}}}. \quad (17)$$

We note that the relative decrease of the mean distance between the particles in the direction of the magnetization is field-dependent through the field-dependence of M_{MF} and that it does not depend explicitly on d_0. It might depend on d_0 through the d_0-dependence of the elastic modulus K_H^{el} and magnetization M_{MF}.

Let us note that the condition to write eqn 14 and 15 now reads $3\mu_0 {M_{\mathrm{MF}}}^2 \ll 4\pi K_H^{\mathrm{el}}$.

In a similar way considering the interaction energy of two parallel dipoles with the radius vector perpendicular to their direction

$$U_{\mathrm{dd}}^{\perp} = \frac{\mu_0 m^2}{4\pi\left(x_{j+1} - x_j\right)^3} \simeq \frac{\mu_0 m^2}{4\pi {d_0}^3} - \frac{3\mu_0 m^2}{4\pi {d_0}^4}\left(x_{j+1} - x_j - d_0\right), \quad (18)$$

we obtain the mean distance between particles in the direction perpendicular to the magnetization of the sample

$$\frac{d_{\perp}}{d_0} = 1 + \frac{3\mu_0 {M_{\mathrm{MF}}}^2}{4\pi K_H^{\mathrm{el}}}. \quad (19)$$

6. Test of the model – a comparison with the experiment

At the highest fields of the experiment M_{MF} is saturated whatever the sample. K_H^{el} can thus be easily evaluated from the relationship $K_H^{\mathrm{el}} = 9\mu_0 M_{\mathrm{MF}}^{\mathrm{sat}^2} d_0/4\pi(\tilde{d}_{\perp} - \tilde{d}_{\parallel})$ deduced from eqn (17) and (19). The values of K_H^{el} (summarized in Table 2) are obtained for each sample from the adjustment of the global H-dependence of $q_{\parallel}^{\max}$ and $q_{\perp}^{\max}$ experimentally measured with the following expression:

$$q_{\parallel}^{\max}(H) = q_0^{\max} \Big/ \left(1 - \frac{3\mu_0 {M_{\mathrm{MF}}}^2(H)}{2\pi K_H^{\mathrm{el}}}\right) \quad \text{and}$$
$$q_{\perp}^{\max}(H) = q_0^{\max} \Big/ \left(1 + \frac{3\mu_0 {M_{\mathrm{MF}}}^2(H)}{4\pi K_H^{\mathrm{el}}}\right) \quad (20)$$

Eqn (20) is also deduced from eqn (17) and (19). The H-dependence of M_{MF} in the concentrated colloids investigated here can be calculated with the characteristics of Table 1 and by using the effective field model[11,15] detailed in Appendix I. As in the mean-field model the NP polydispersity is not taken into account, an averaged magnetic NP diameter $\sqrt[3]{\langle {d_{\mathrm{NP}}}^3\rangle}$ is used here (= 11.5 nm for sample A for example in Fig. 5) because the magnetic moment μ entering in the reduced variable ξ is proportional to the NP volume. The model describes our data well. In Fig. 5a the same value $K_H^{\mathrm{el}} = 2.6 \times 10^4$ Pa is used for the adjustments of $q_{\parallel}^{\max}(H)$ and $q_{\perp}^{\max}(H)$ in both directions parallel and perpendicular to the applied field. Table 2 shows the K_H^{el} values determined in this way for all the samples tested here. These under-field K_H^{el} values are of the same order of magnitude as the bulk modulus B_0 determined in zero field in Section 3.

They are however systematically larger by a factor of the order of a few units.

The under-field anisotropy of the magnetic dipolar interaction between adjacent NPs in the magnetic fluid can be expressed in terms of SAXS determined quantities as:

$$\frac{U_{dd}^{\perp} - U_{dd}^{\parallel}}{k_B T} = \frac{3\mu_0}{4\pi}\frac{M_{MF}^{2}(H) d_0^{2}}{k_B T} = \frac{K_H^{el}}{3k_B T} d_0^{2}(d_{\perp} - d_{\parallel}) \qquad (21)$$

Fig. 6 shows the plots of $S_{\perp}^{max}(H) - S_{\parallel}^{max}(H)$ as a function of $K_H^{el} d_0^{2}(d_{\perp} - d_{\parallel})/3k_B T$ for the fluid samples in Table 1. It shows that the anisotropy of $S^{max}(H)$ is proportional to the anisotropy of $U_{dd}(H)$ with $S_{\perp}^{max}(H) - S_{\parallel}^{max}(H) = \alpha(U_{dd}^{\perp} - U_{dd}^{\parallel})$ and the same experimental coefficient $\alpha \sim 0.7$ whatever $[cit]_{free}$ in the dispersion. This coefficient decreases to 0.3 in the case of the glass forming sample B (data not shown). Another sample comparable to sample C was studied under a magnetic field by SANS in ref. 9. It scales the same way with $\alpha \sim 0.7$.

In Fig. 5b, $S_{\parallel}^{max}$ and $S_{\perp}^{max}$ are fitted with:

$$S_{\parallel}^{max}(H) = S_0^{max} - \alpha\frac{\mu_0 M_{MF}^{2}(H)}{2\pi k_B T} d_0^{3} \quad \text{and}$$
$$S_{\perp}^{max}(H) = S_0^{max} + \alpha\frac{\mu_0 M_{MF}^{2}(H)}{4\pi k_B T} d_0^{3} \qquad (22)$$

with $\alpha = 0.7$ and $M_{MF}(H)$ adjusted as in Fig 5a.

Another graphical representation of these results, strictly equivalent to the previous analysis, consists of plotting the different ways of deducing the quantity $\frac{3\mu_0 M_{MF}^{2}}{2\pi K_H^{el}}$ as eqn (17), (19) and (22) can be rewritten as:

$$\frac{3\mu_0 M_{MF}^{2}}{2\pi K_H^{el}} = 1 - \frac{d_{\parallel}}{d_0} = 2\left(\frac{d_{\perp}}{d_0} - 1\right) = \frac{2k_B T\left(S_{\perp}^{max}(H) - S_{\parallel}^{max}(H)\right)}{\alpha K_H^{el} d_0^{3}} \qquad (23)$$

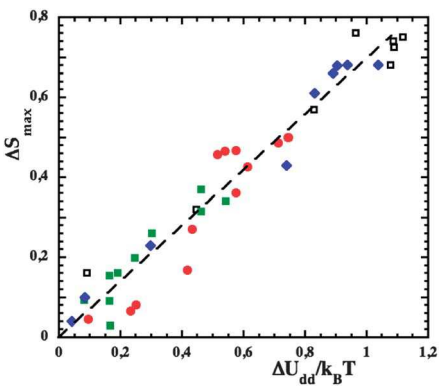

Fig. 6 $S_{\parallel}^{max} - S_{\perp}^{max}$ as a function of the reduced quantity $\frac{U_{dd}^{\perp} - U_{dd}^{\parallel}}{k_B T} = \frac{K_H^{el}}{3k_B T} d_0^{2}(d_{\perp} - d_{\parallel})$ calculated with the experimental values of d_0, $d_{\perp}$ and $d_{\parallel}$ and with K_H^{el} from Table 2. Symbols: sample A (closed discs), sample C (closed squares), sample D (closed diamonds), and sample E (open squares). The dashed line corresponds to $S_{\parallel}^{max} - S_{\perp}^{max} = 0.7\ \frac{U_{dd}^{\perp} - U_{dd}^{\parallel}}{k_B T}$.

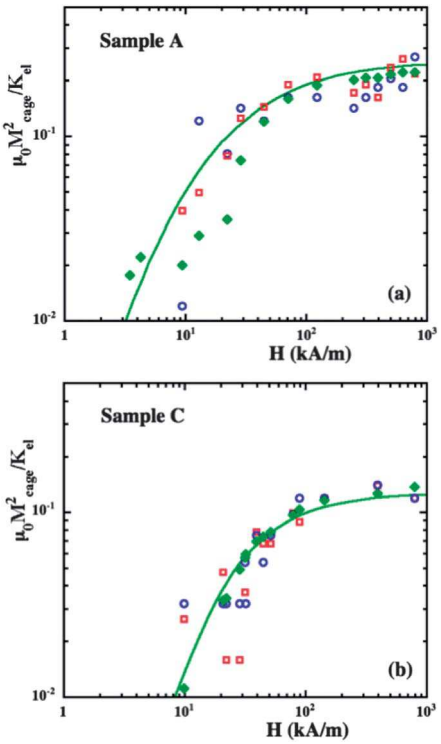

Fig. 7 Field dependence of $3\mu_0 M_{MF}^{2}/2\pi K_H^{el}$ for sample A (a) and for sample C (b) obtained in different ways (see eqn (23)): (i) as equal to $1 - d_{||}/d_0$ using $q_{\parallel}^{max}$ and q_0^{max} measurements (open squares), (ii) as equal to $2(d_{\perp}/d_0 - 1)$ using $q_{\perp}^{max}$ and q_0^{max} measurements (open discs) and (iii) as equal to $(S_{\perp}^{max}(H) - S_{\parallel}^{max}(H))\frac{2k_B T}{\alpha K_H^{el} d_0^{3}}$ using $S_{\perp}^{max}$ and $S_{\parallel}^{max}$ measurements (closed diamonds with $\alpha = 0.7$ and K_H^{el} from Table 2). The full lines correspond to the calculation of $3\mu_0 M_{MF}^{2}/2\pi K_H^{el}$ with M_{MF}^{2} calculated with the effective field model of Appendix I (with $d_{NP} = 11.5$ nm for both samples A and C) and the values of K_H^{el} from Table 2.

Fig. 7 shows the comparison, for sample A in Fig 7a and sample C in Fig 7b, of the H-dependence of the three experimental quantities:

(i) $\left(1 - \frac{d_{\parallel}}{d_0}\right)$ deduced from the H-dependence of $q_{||}(H)$,

(ii) $2\left(\frac{d_{\perp}}{d_0} - 1\right)$ deduced from the H-dependence of $q_{\perp}(H)$,

(iii) $2k_B T(S_{\perp}^{max}(H) - S_{\parallel}^{max}(H))/0.7K_H^{el} d_0^{3}$.

All three superimpose with $3\mu_0 M_{MF}^{2}/2\pi K_H^{el}$ as deduced from the effective field model of Appendix I with the K_H^{el} values of Table 2 (full line in Fig. 7). In this figure it is easy to verify that the condition $3\mu_0 M_{MF}^{2} \ll 2\pi K_H^{el}$, which allows us to write eqn 14–17, is here fulfilled for samples A and B. This is true for all the samples in Table 2. This representation also clearly shows the great coherence of the experimental data in parallel and perpendicular directions both for the q^{max} position of the $S(q)$ peak and for the value of its maximum S^{max}.

7. Discussion – limits of the model

Let us go back to the under-field profiles of $S_{\perp}(q)$ and $S_{||}(q)$ of Fig. 1b from sample A at $H = 500$ kA m^{-1}. Besides the anisotropy of q^{max} and S^{max}, the bump of $S(q)$ obviously presents also a width anisotropy. This could eventually originate from an

experimental under-field anisotropy of σ in contrast to what is assumed in the model of Sections 5 and 6.

We thus make the hypothesis that we can analyze the under-field profiles in Fig. 1b with eqn (4) and define $\sigma_{||}(H)$ and $\sigma_{\perp}(H)$ in the two directions. Adjusting the coordinates of the maxima of $S_{||}(H)$ and $S_{\perp}(H)$ while fitting them with eqn (4), we find for sample A at $H = 500$ kA m^{-1} (see Fig. 8) $\sigma_{||} = 5.56$ nm and $\sigma_{\perp} = 4.35$ nm. For every field H we find a reasonable agreement for $3(\sigma_0/d_0)^2 \sim (\sigma_{||}/d_{||})^2 + 2(\sigma_{\perp}/d_{\perp})^2$. The field-dependence of $\sigma_{||}$ and $\sigma_{\perp}$ is presented in Fig. 9 where it is tentatively adjusted to $M_{MF}{}^2$ (see the figure caption).

Note that the σ values (σ_0, $\sigma_{||}$ and $\sigma_{\perp}$) are all of the same order of magnitude, but systematically larger than the width $\sigma_H = \sqrt{k_B T/K_H^{el} d_0} = 3.1$ nm that is deduced from the under-field model in Section 6 for this sample (using eqn (16) and the sample characteristics in Table 2, particularly the value of K_H^{el}).

This subsidiary H-dependence of σ could eventually be due to the long range dipolar interaction which introduces a supplementary force in the direction parallel to the field.[9,11,12,14,15] Indeed at very low q's, thus on the macroscopic scale, this supplementary force explains well the experimental structure factor anisotropy $S_{||}{}^{-1}(q=0) - S_{\perp}{}^{-1}(q=0)$ and its H-dependence. Here $S_{||}{}^{-1}(q=0) - S_{\perp}{}^{-1}(q=0)$ is maximum in large fields where it equals ~11. This value is comparable to $\gamma = \Psi_{dd}\Phi = 9.8$ (see Table 1 and Appendix I) as expected from ref. 9, 11, 12, 14 and 15. Note that the fits of $S_{||}(q)$ and $S_{\perp}(q)$ by eqn (4) are adjusted here to the maximum of $S(q)$. As shown in Fig. 8 they are unable to model the low-q's anisotropy observed in the experiments.

We now compare sample A and sample B. They are based on the same nanoparticles but sample A is a fluid sample[9] while sample B is a (freshly prepared) glass-forming one as in ref. 18 and 35 with a much larger compression modulus B_0. Table 3 shows the comparison, for these two samples, of the large field anisotropies of d, S^{max} and σ.

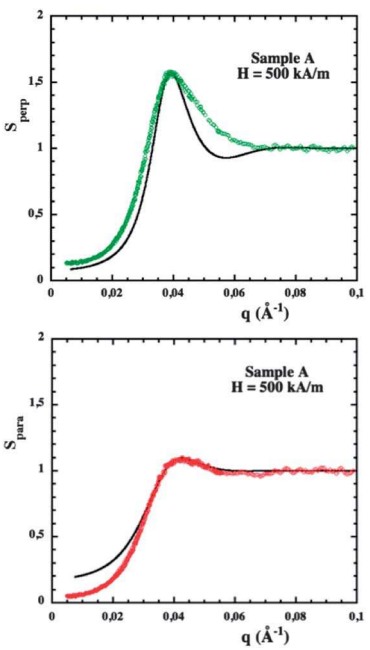

Fig. 8 Under-field $S(q)$ profiles of sample A: $S_{\perp}(q)$ in (a) and $S_{||}(q)$ in (b) adjusted with eqn (4) with respectively $(\sigma_{\perp}/d_{\perp})^2 = 0.07$ and $(\sigma_{||}/d_{||})^2 = 0.14$. (Open dots are the experimental data, full lines are their theoretical adjustment with eqn (4)).

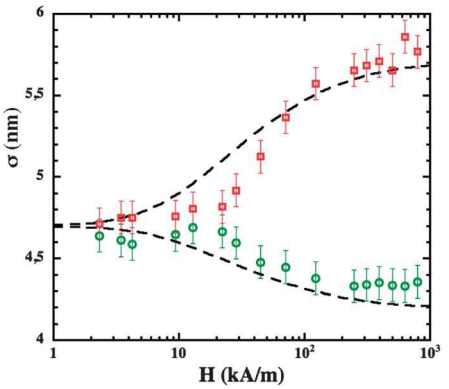

Fig. 9 Under-field σ-anisotropy of sample A deduced from fitting the profiles $S_{\perp}(H)$ and $S_{||}(H)$ by eqn (4) with an adjustment of $S_{\perp}^{max}(H)$ and $S_{||}^{max}(H)$. Symbols: $\sigma_{\perp}$ (open discs) and $\sigma_{||}$ (open squares); the dashed line corresponds to $\sigma_{||} - \sigma_0 = 2(\sigma_0 - \sigma_{\perp}) \propto M_{MF}{}^2$ adjusted with a constant coefficient and with the field dependence of M_{MF} deduced from the effective field model of Appendix I as in Fig. 5 and 7a.

If a comparable anisotropy of d (and q^{max}) is observed with both samples, the anisotropy of S^{max} is reduced by a factor of 2 in sample B with respect to that of the fluid sample A. By adjusting the under-field $S(q)$ profiles of sample B with eqn (4), we observe that the under-field σ-anisotropy is also strongly reduced (see Table 3). Moreover we can note that the under-field anisotropy of $S(q=0)$, if any, is not detected experimentally and that the value $\sigma_0 = 2.3$ nm deduced from the compressibility determination is here close to the value $\sigma = 1.9$ nm deduced from our under-field model in Sections 5 and 6.

The cage model developed in Sections 5 and 6 is thus very well adapted to an almost "solid" sample as sample B which presents a very low compressibility ($\chi_{T,0} = 0.04$). This point has been checked with several "fresh" solid samples. However under these glassy conditions, such "freshly prepared" samples[18] present ageing with time and slow dynamics[26] which are also anisotropic under an applied field.[35] The heterogeneous nature of this dynamics has been demonstrated in zero field.[36] One could eventually hypothesize that, in that case, the under-field anisotropy of σ transforms into an anisotropy of the heterogeneities. This remains to be studied in close relationship with the local anisotropies evidenced here in the probed concentrated systems.

Table 3 Maximum anisotropies of d, S^{max} and σ determined in large magnetic fields from the scattering patterns for samples A and B and deduced from the adjustment of the $S(q)$ profiles with eqn (4)

Sample	$\frac{\tilde{d}_{\perp} - \tilde{d}_{||}}{d_0}$	$\frac{\tilde{S}_{\perp}^{max} - \tilde{S}_{||}^{max}}{S_0^{max}}$	$\frac{\tilde{\sigma}_{\perp} - \tilde{\sigma}_{||}}{\sigma_0}$
A – fluid	8.9%	37%	30%
B – glass forming	7.7%	18%	3%

8. Conclusion

The structure factor $S(\vec{q})$ of concentrated aqueous magnetic fluids is here experimentally determined by SAXS and SANS in the case where the interparticle interactions are repulsive on average. The various experiments are performed under controlled conditions of electrostatic repulsion (constant ionic strength) and NP size (using several samples of similar NP diameter). By comparing, in zero applied field, the compressibility of the system and the q_{max} value associated with the $S(q)$ maximum we determine (i) the cage dimension (spherical on average), (ii) the mean quadratic displacement of the NPs and (iii) the bulk modulus of the system as a function of the NP volume fraction. Under an applied field, the interparticle interaction remains always repulsive but becomes anisotropic because of the magnetic dipolar interaction contribution and the structure factor then presents anisotropic features on the scale of $2\pi/q_{max}$. SAXS experiments show that the cage becomes anisotropic and presents an oblate deformation at almost constant volume.

To describe these local anisotropic features, we develop a formalism connecting the magnetic and under-field elastic characteristics of the magnetic NP system with the values of the scattering vector $q_{\parallel}^{max} = \frac{2\pi}{d_{\parallel}}$ and $q_{\perp}^{max} = \frac{2\pi}{d_{\perp}}$ at the maxima of $S(\vec{q})$, defined respectively in the direction of and normal to the applied field $\vec{H}$. This formalism is based on the elastic deformation of the cage at constant volume under the applied field. On the scale of the maximum of the structure factor, this model catches the essence of the q^{max} and S^{max} anisotropies observed here and allows us to deduce the (Young's) elastic modulus of the magnetic fluid associated with its under-field deformation. This Young's modulus is of the same order of magnitude as the zero-field bulk modulus and is larger by a factor of the order of a few units.

However under-field we experimentally observe the anisotropy of the mean quadratic displacement of the NPs around their mean position, which is not captured by the model. At very high volume fraction this feature is strongly damped and almost disappears as the sample is becoming glass-forming with a very low compressibility and a large bulk modulus. It will be interesting in the near future to probe the slow dynamics of such glassy systems, perturbed in an anisotropic way with an applied magnetic field.

Appendix I: an effective field model of the magnetic fluid magnetization M_{MF}

To take into account the magnetic interparticle interaction under a magnetic field, an effective field model has been developed in the framework of a mean field approximation[11,15] to describe the magnetization M_{MF} of concentrated magnetic fluids:

$$M_{MF} = \Phi m_S L(\xi_e) \tag{24}$$

where Φ is the MF volume fraction, m_S is the nanoparticle saturation magnetization, $L(\xi_e) = \coth(\xi_e) - \xi_e^{-1}$ the Langevin function with ξ_e being the effective Langevin parameter given by the self-consistent equation:

$$\xi_e = \xi + \lambda\gamma L(\xi_e) \tag{25}$$

with $\xi = \mu_0 m_s H\pi {d_{NP}}^3/6k_BT$, λ is the effective field constant and γ is the dipolar interaction parameter of the dispersion defined here as $\gamma = \mu_0 {m_s}^2 \Phi\pi {d_{NP}}^3/6k_BT$. In ξ, we use the average $\sqrt[3]{\langle {d_{NP}}^3\rangle}$ computed over the whole diameter distribution in each sample, as ξ scales as ${d_{NP}}^3$. The effective field constant λ has been determined to be 0.22 in previous experimental studies on similar magnetic fluids,[11,15] as well in numerical simulations.[38] The parameter $\Psi_{dd} = \gamma/\Phi$ is characteristic of the nanoparticles. It is experimentally determined in ref. 13 (see Table 1) by the measurement of the initial susceptibility $\chi_0 = M/H$ of dispersions at low concentrations for which $\gamma = 3\chi_0$ and $\Psi_{dd} = 3\chi_0/\Phi$.

Appendix II: Carnahan–Starling osmotic compressibility

The NP's in this work bear a negative superficial charge which produces a strong electrostatic interparticle repulsion. The Carnahan–Starling formalism[37] is usually used to describe hard sphere systems (HS). In the present case the osmotic pressure of the NP's system can be also described in this framework, if effective spheres are introduced in the term correcting the perfect gas expression of the osmotic pressure.[18,20] By introducing the screening length κ^{-1} of the NP's system, the volume of these effective spheres is $\frac{\pi}{6}(d_{NP} + 2\kappa^{-1})^3$ (instead of $V_{NP} = \frac{\pi}{6}{d_{NP}}^3$) and their volume fraction is Φ_{eff} (instead of Φ). The osmotic pressure then is expressed as:

$$\Pi V_{NP} = k_B T \Phi Z_{CS}(\Phi_{eff}) \quad \text{with}$$
$$Z_{CS}(\Phi_{eff}) = \frac{1 + \Phi_{eff} + {\Phi_{eff}}^2 - {\Phi_{eff}}^3}{(1 - \Phi_{eff})^3}. \tag{26}$$

with $\Phi_{eff} \sim \Phi\left(1 + \frac{2\kappa^{-1}}{d_{NP}}\right)^3$. The osmotic compressibility, being defined as:

$$\chi_{T,0} = \frac{k_B T}{(\partial\Pi V_{NP}/\partial\Phi)_T} = \frac{1}{Z_{CS}\left(1 + \frac{\Phi_{eff}}{Z_{CS}}\frac{\partial Z_{CS}}{\partial\Phi_{eff}}\right)} \tag{27}$$

can be written as a function of Φ_{eff} as:

$$\chi_{T,0} = \frac{(1 - \Phi_{eff})^4}{1 + 4\Phi_{eff} + 4{\Phi_{eff}}^2 - 4{\Phi_{eff}}^3 + {\Phi_{eff}}^4}. \tag{28}$$

This expression is compared in Fig. 2b with the experimental determination of $\chi_{T,0}$ using $\Phi_{eff} \sim 1.9\Phi$ and $\kappa^{-1} \sim 1.2$ nm, close to the evaluations in ref. 18. It fits well with the experimental values up to $\Phi \sim 20\%$ thus up to $\Phi_{eff} \sim 38\%$, close to the customary value for such an effective H. S. model.[39]

Acknowledgements

We acknowledge ESRF for the beamtime allocation on the ID02 beamline, our local contact P. Panine together with V. Dupuis

and T. Narayanan for their help during the experiment. This work was supported by the international PHC program OSMOSE no. 22497YE, the GDRE GAMAS, the direction of UPMC International Relations and the "Fédération 21 de l'UPMC – Dynamique des Systèmes Complexes".

References

1 *Magnetic Fluids and Applications HandBook*, ed. B. Berkovsky, Begell House, New York, 1996.
2 *Magnetically controllable Fluids and their Applications*, ed. S. Odenbach, Springer, Berlin, 2003.
3 R. E. Rosensweig, *Ferrohydrodynamics*, Cambridge University Press, Cambridge, 1985.
4 E. Blums, A. Cēbers and M. M. Maiorov, *Magnetic Fluids*, de Gruyter, New York, 1997.
5 W. Drenckhan, F. Elias, S. Hutzler, D. Weaire, E. Janiaud and J.-C. Bacri, *J. Appl. Phys.*, 2003, **93**, 1078.
6 E. Janiaud, J.-C. Bacri, A. Cebers and F. Elias, *J. Magn. Magn. Mater.*, 2005, **289**, 215.
7 M. Klokkenburg, B. H. Erné, A. Wiedenmann, A. V. Petukhov and A. P. Philipse, *Phys. Rev. E: Stat., Nonlinear, Soft Matter Phys.*, 2007, **75**, 051408.
8 R. Stanway, J. L. Sproston and A. K. El-Wahed, *Smart Mater. Struct.*, 1996, **5**, 464.
9 G. Mériguet, F. Cousin, E. Dubois, F. Boué, A. Bourdon, A. Cēbers, B. Farago and R. Perzynski, *J. Phys. Chem. B*, 2006, **110**, 4378.
10 J. Wagner, B. Fischer and T. Autenrieth, *J. Chem. Phys.*, 2006, **124**, 114901.
11 F. Gazeau, E. Dubois, J.-C. Bacri, F. Boué, A. Cēbers and R. Perzynski, *Phys. Rev. E: Stat., Nonlinear, Soft Matter Phys.*, 2002, **65**, 031403.
12 F. Gazeau, F. Boué, E. Dubois and R. Perzynski, *J. Phys.: Condens. Matter*, 2003, **15**, S1305.
13 G. Mériguet, E. Wandersman, E. Dubois, A. Cēbers, J. de Andrade Gomes, G. Demouchy, J. Depeyrot, A. Robert and R. Perzynski, *Magnetohydrodynamics*, 2012, **48**, 415.
14 A. Cēbers, *Magnetohydrodynamics*, 1982, **18**, 137.
15 J. C. Bacri, A. Cēbers, A. Bourdon, G. Demouchy, B. M. Heegaard and R. Perzynski, *Phys. Rev. Lett.*, 1995, **74**, 5032.
16 K. I. Morozov, *Phys. Rev. E: Stat., Nonlinear, Soft Matter Phys.*, 1996, **53**, 3841.
17 J. J. Cerda, E. Elfimova, V. Ballenegger, E. Krutikova, A. Ivanov and C. Holm, *J. Magn. Magn. Mater.*, 2011, **323**, 1246.
18 E. Wandersman, V. Dupuis, E. Dubois and R. Perzynski, *Phys. Rev. E: Stat., Nonlinear, Soft Matter Phys.*, 2009, **80**, 041504.
19 E. Dubois, F. Boué, V. Cabuil and R. Perzynski, *J. Chem. Phys.*, 1999, **111**, 7147.
20 F. Cousin, E. Dubois and V. Cabuil, *Phys. Rev. E: Stat., Nonlinear, Soft Matter Phys.*, 2003, **68**, 021405.
21 R. Massart, E. Dubois, V. Cabuil and E. Hasmonay, *J. Magn. Magn. Mater.*, 1995, **149**, 1.
22 G. Mériguet, E. Dubois, M. Jardat, A. Bourdon, G. Demouchy, V. Dupuis, B. Farago, R. Perzynski and P. Turq, *J. Phys.: Condens. Matter*, 2006, **18**, S2685.
23 M. F. Islam, K. H. Lin, D. Lacoste, T. C. Lubensky and A. G. Yodh, *Phys. Rev. E: Stat., Nonlinear, Soft Matter Phys.*, 2003, **67**, 021402.
24 A. Mertelj, L. Cmok and M. Copič, *Phys. Rev. E: Stat., Nonlinear, Soft Matter Phys.*, 2009, **79**, 041402.
25 G. Mériguet, E. Dubois, V. Dupuis and R. Perzynski, *J. Phys.: Condens. Matter*, 2006, **18**, 10119.
26 A. Robert, E. Wandersman, E. Dubois, V. Dupuis and R. Perzynski, *Europhys. Lett.*, 2006, **75**, 764.
27 E. Wandersman, E. Dubois, V. Dupuis, R. Perzynski, *Proc. of the 11th French-Japanese Int. Seminar on Magnetic Fluids, Kyoto, Japan*, 11-14 2005.
28 G. Mériguet, PhD dissertation, Univ. Paris 6-France, 2005.
29 E. Wandersman, PhD dissertation, Univ. Paris 6-France, 2007.
30 P. Schall, D. A. Weitz and F. Spaepen, *Science*, 2007, **318**, 1895.
31 H. Matsuoka, H. Tanaka, T. Hashimoto and N. Ise, *Phys. Rev. B: Condens. Matter Mater. Phys.*, 1987, **36**, 1754.
32 P. M. Chaikin, and T. C. Lubensky, *Principles of condensed matter physics*, Cambridge University Press, Cambridge, 1995.
33 A. Cēbers, Z. Dogic and P. A. Janmey, *Phys. Rev. Lett.*, 2006, **96**, 247801.
34 L. D. Landau, and E. M. Lifshitz, *Electrodynamics of continous media*, Nauka, Moscow, 1982.
35 E. Wandersman, Y. Chushkin, E. Dubois, V. Dupuis, G. Demouchy, A. Robert and R. Perzynski, *Braz. J. Phys.*, 2009, **39**, 210.
36 E. Wandersman, A. Duri, A. Robert, E. Dubois, V. Dupuis and R. Perzynski, *J. Phys.: Condens. Matter*, 2008, **20**, 155104.
37 N. F. Carnahan and K. E. Starling, *J. Chem. Phys.*, 1970, **53**, 600.
38 M. Mériguet, M. Jardat and P. Turq, *J. Chem. Phys.*, 2005, **123**, 14915.
39 A. Vrij, J. W. Jansen, J. K. G. Dhont, C. Pathmamanoharan, M. M. Kops-Werkhoven and F. M. Funaut, *Faraday Discuss. Chem. Soc.*, 1983, **76**, 19.